PNAS RESEARCH ARTICLE | PHYSICS

Strong intrinsic multiferroism and magnetoelectric coupling in (1–x)$BiFeO_3$–(x)$BaTiO_3$ films

Tae Yeon Kim[a,b], Jesse Schimpf[b,c], Atanu Paul[d], Michael Xu[e], Atanu Samanta[d,f], Sajid Husain[c,g], Peter Meisenheimer[c], Isaac Harris[g,h], Peter Finkel[i], Thomas Mion[j], Margo Staruch[j], Anthony J. Ruffino[j,k], Stefan Masiuk[j], Liyan Wu[j], Tae Joon Park[c,l], Deokyoung Kang[b,c], Christoph Klewe[g], Paul Stevenson[m], Ramamoorthy Ramesh[a,b,c,n,1], Andrew M. Rappe[f], James M. LeBeau[e], Jonathan E. Spanier[j,k], Ilya Grinberg[d], and Lane W. Martin[a,b,n,o,1]

Affiliations are included on p. 9.

Contributed by Ramamoorthy Ramesh; received January 29, 2026; accepted April 1, 2026; reviewed by John T. Heron and Chan-Ho Yang

The coexistence of ferroelectric and antiferromagnetic order in $BiFeO_3$ makes it promising for next-generation magnetoelectric devices. But, single-phase multiferroics with robust room-temperature polarization and magnetization are rare. Here, enhanced, room-temperature ferroelectric polarization (≈ 120 μC cm^{-2}), saturation magnetization (≈ 40 emu cm^{-3}), and strong magnetoelectric coupling (≈ 400 mV cm^{-1} Oe^{-1}) are observed in epitaxial (1–x)$BiFeO_3$–(x)$BaTiO_3$ thin films. These values of magnetization and magnetoelectric coupling are, respectively, one- and two-orders of magnitude larger than those same properties in the widely studied parent material $BiFeO_3$. This sought after combination of properties is found in a distinct tetragonal phase, which is different from rhombohedral and super-tetragonal variants of $BiFeO_3$, that emerges at x = 0.2 to 0.3 via combined chemical substitution and epitaxial strain. Structural and physical-property characterization, along with first-principles calculations, reveal a transition from monoclinic to tetragonal symmetry and suggest that short-range ordering of the titanium in the tetragonal phase results in ferrimagnetic spin ordering. This work demonstrates a unique single-phase multiferroic combining strong polarization, magnetization, and magnetoelectric coupling achieved through manipulation of the coupled chemical order and spin order; thereby addressing a major challenge in multiferroics research and providing a path toward practical room-temperature, efficient charge-to-spin and spin-to-charge conversion technologies.

multiferroic | single-phase | epitaxial thin-film | magnetoelectric coupling

Significance

Materials that can efficiently couple electric and magnetic properties are central to next-generation, low-power information technologies, yet such behavior rarely persists at room temperature in a single phase. Here, a distinct tetragonal phase of (1–x)$BiFeO_3$–(x)$BaTiO_3$ that simultaneously exhibits strong ferroelectric polarization, enhanced magnetization, and exceptionally large magnetoelectric coupling at ambient conditions is achieved. Unlike conventional multiferroics, where one or more properties are weak or require low temperatures to access, these effects emerge intrinsically through a combination of chemical substitution and epitaxial strain. This work establishes a practical pathway for engineering room-temperature multiferroics and provides a foundation for efficient electric-field control of magnetism in future spintronic and energy-efficient electronic devices.

Multiferroics have attracted considerable attention due to their complex physics and potential for application in next-generation logic-in-memory. The most widely studied single-phase multiferroic system is $BiFeO_3$, with a rhombohedral perovskite structure and robust polarization along the pseudocubic <111> (~100 μC cm^{-2}, corresponding to polarization of ~65 μC cm^{-2} along the <001>) and G-type antiferromagnetic order [which can support a long-period (≈ 62 nm) spin cycloid] (1–3). In thin-film form, researchers have observed weak ferromagnetic-like response (producing moments of 4 to 8 emu cm^{-3}) (2–4), arising from a small (≈ 1°) canting of the spins, originating from the Dzyaloshinskii–Moriya interaction and coupled to the polarization (5). While fundamentally interesting, such a magnetization is too small to be of practical use for magnetic-based devices (6) and, instead, the coupling between the ferroelectric and antiferromagnetic order has been leveraged to achieve electric-field control of ferromagnetism via exchange interactions with coupled ferromagnetic layers (7–10). Despite such work, the advantages of a single-phase multiferroic material with robust intrinsic magnetoelectric coupling have motivated an intense search for materials with robust ferroelectric and ferromagnetic(-like) properties (and coupling between them) at room temperature; to date, this combination of properties has remained elusive.

Many strategies have been explored to realize robust single-phase multiferroicity including considerable work to modify the polar and magnetic order in $BiFeO_3$ and even take advantage of its polymorphic tendency (i.e., it can be stabilized in several different phases) (11–13). For example, under sufficiently large tensile strains ($\gtrsim$2.5%, relative to bulk), an orthorhombic phase is produced (13, 14) and under sufficiently large compressive strains ($\lesssim$–4.5%, relative to bulk) a "super-tetragonal-like" (actually triclinic) phase is obtained (14–16). This super-tetragonal-like structure, with a large c/a lattice parameter ratio (≈ 1.25) and a predicted polarization as large as ~150 μC cm^{-2} (17), has been the subject of much study, but it has been found that growing a phase-pure version of this material is challenging as it is limited to ultrathin films (e.g., <10 nm) (18) unless exceptional steps are taken (19). Alternatively, chemical substitution for bismuth (with rare-earths such as Gd^{3+} and Sm^{3+} or alkaline earth

Reviewers: J.T.H., University of Michigan; and C.-H.Y., Korea Advanced Institute of Science and Technology.

The authors declare no competing interest.

[1]To whom correspondence may be addressed. Email: rramesh@berkeley.edu or lwmartin@rice.edu.

This article contains supporting information online at https://www.pnas.org/lookup/suppl/doi:10.1073/pnas.2603475123/-/DCSupplemental.

Published April 28, 2026.

metals such as Ba^{2+}) or iron (with transition metals such as Mn^{2+}, Ti^{4+}, or Co^{2+}) has also been used to modify the crystal structure and dielectric, ferroelectric, and magnetic properties (11, 20–22), but this has not yielded simultaneous robust ferroelectric and magnetic properties. Alloying with $BaTiO_3$ (tetragonal symmetry; a = 4.004 Å, c = 4.024 Å) has been shown to simultaneously impact both the polar and magnetic properties of $BiFeO_3$. In $(1–x)BiFeO_3–(x)BaTiO_3$ ceramics, increasing the $BaTiO_3$ content drives an increase in the out-of-plane lattice parameter, the c/a ratio, and the structural distortion angle (which reaches 90°) resulting in a transformation from rhombohedral to tetragonal structure for $x \gtrsim 0.3$ (23, 24). It has also been suggested that alloying with nonmagnetic $BaTiO_3$ can produce a net magnetization by suppressing the spiral-spin structure, which can lead to long-range magnetic ordering at low temperatures (25, 26) (albeit with a small magnetization of ≈ 5 emu cm^{-3}). Despite such studies, the production of a single-phase $BiFeO_3$-derived system with simultaneous large ferroelectric and magnetic nature (and strong coupling between them) remains a challenge.

Here, epitaxial strain and chemical substitution are combined in $(1–x)BiFeO_3–(x)BaTiO_3$ films to achieve this long-sought-after combination of robust ferroelectric and ferromagnetic-like response with strong, intrinsic magnetoelectric coupling. The resulting tetragonal phase is distinct from that of the rhombohedral parent and highly strained "super-tetragonal-like" versions of $BiFeO_3$. Using a combination of thin-film epitaxy, extensive structural and physical-property measurements, and first-principles calculations, it is demonstrated that simultaneous control of chemistry and epitaxial strain drives the evolution from a rhombohedral-like monoclinic structure at x = 0 to 0.05 to a tetragonal structure distinct from previously reported ones at x = 0.2 to 0.3. The tetragonal phase also has an enhanced polarization (≈ 120 μC cm^{-2}) and an order-of-magnitude larger saturation magnetization (≈ 40 emu cm^{-3}) as compared to parent $BiFeO_3$. A ferrimagnetism-based mechanism for this increased magnetic moment is explored using first-principles calculations. Finally, the room-temperature magnetoelectric coefficient for the tetragonal phase is measured to be ≈ 400 mV cm^{-1} Oe^{-1}; nearly two orders magnitude higher than that measured in $BiFeO_3$. This work provides evidence for a single-phase multiferroic with robust polarization and magnetization and large magnetoelectric coupling at room temperature.

Results

A Distinct Tetragonal Structure in $BiFeO_3$-Based Films. Epitaxial thin-film heterostructures of $(1–x)BiFeO_3–(x)BaTiO_3$ (x = 0, 0.05, 0.1, 0.2, and 0.3) were deposited using pulsed-laser deposition on $SrRuO_3$-buffered $GdScO_3$ [110], $DyScO_3$ [110], and $SrTiO_3$ [001] substrates (*Materials and Methods*). Henceforth, these films will be referred to by their $BaTiO_3$ content (e.g., x = 0.2 films) and the substrate will be included for disambiguation only as required. X-ray diffraction studies reveal a gradual phase transition wherein the out-of-plane lattice parameter expands with both strain (ε) and $BaTiO_3$ content for films grown on $GdScO_3$ [110] ($\varepsilon = 0.05\%$), $DyScO_3$ [110] ($\varepsilon = -0.35\%$) (*SI Appendix*, Fig. S1 *A* and *B*), and $SrTiO_3$ [001] ($\varepsilon = -1.35\%$) (Fig. 1*A*) substrates, reaching the highest out-of-plane lattice-parameter values for x = 0.2 and 0.3 films grown on $SrTiO_3$ and scandate substrates, respectively. While it was possible to produce similar phases on all substrates studied herein, for brevity the remaining discussion focuses on films grown on $SrTiO_3$ [001] since they allow for the widest array of subsequent studies. Reciprocal space mapping studies (Fig. 1*B* and *SI Appendix*, Fig. S1 *C–G*) show that all films (x = 0-0.3) deposited on $SrTiO_3$ [001] substrates are coherently strained to the substrate and allow for extraction of the in-plane (a) and out-of-plane (c) lattice constants (Fig. 1*C*), c/a ratio (Fig. 1*D*), and monoclinic angle β (Fig. 1*E*) as a function of $BaTiO_3$ content. An evolution from a rhombohedral-derived monoclinic structure (M_A; with c = 4.015 Å, c/a = 1.03, and β = 89.4° for x = 0 films) to a tetragonal-derived monoclinic structure (M_C; with c = 4.125 to 4.167 Å, c/a = 1.06 to 1.07, and β = 89.6 to 89.9° for x = 0.05 to 0.1 films) to a tetragonal structure (T; with c = 4.242 Å, c/a = 1.09, and β = 90° for x = 0.2 to 0.3 films) (*SI Appendix*, Figs. S3 and S4 and section S1) is observed. The tetragonal structure is distinct from the previously reported super-tetragonal-like phase in x = 0 films grown on $LaAlO_3$ [001] substrates ($c/a \approx 1.23$) (8) and can be maintained up to a film thickness of at least 200 nm (*SI Appendix*, Fig. S1*H*), suggesting that it is more thermodynamically favored as compared to the previously reported metastable phases.

Further details of the structure are revealed by cross-sectional, atomic resolution high-angle annular dark-field (ADF) scanning transmission electron microscopy (HAADF-STEM) of the x = 0.1 (*SI Appendix*, Fig. S5) and 0.2 (Fig. 1 *F–H*) films. All films were found to be solid solutions of high quality and show pristine interfaces with the $SrRuO_3$ bottom electrodes. Atomic-resolution imaging also allows for determination of atom-column positions and mapping of the local tetragonality and polar displacements. For the x = 0.1 films, such mapping reveals polar displacements that deviate from the surface normal and an overall $c/a > 1$, consistent with the macroscopic monoclinic structure seen in the X-ray results (*SI Appendix*, Fig. S7 and section S3). For the x = 0.2 films (Fig. 1*G*), the overall polar displacement lies along the out-of-plane [001], consistent with a tetragonal structure, with a c/a ratio across the film matching that obtained from the X-ray diffraction results. Further, from simultaneously acquired ADF and integrated differential phase contrast (iDPC) images, extraction of local oxygen octahedral tilts/rotation along the $[110]_{pc}$ (i.e., $[100]_o$ of the $SrRuO_3$, where "pc" refers to pseudocubic and "o" to orthorhombic indices) is possible (Fig. 1*H*). For the x = 0.1 films, octahedral tilts are observed to continue across the film–$SrRuO_3$ interface with tilt values as large as 6 to 8°; similar to the octahedral tilting in x = 0 films (*SI Appendix*, Fig. S5 *C* and *D*). Conversely, for x = 0.2 films (Fig. 1*I*), the oxygen octahedral tilt angles are no longer coupled across the film–$SrRuO_3$ interface and approach zero, consistent with a tetragonal structure. Additional *B*-site-normalized intensity mapping results from HAADF-STEM images (*SI Appendix*, Fig. S8) are also provided. Piezoresponse force microscopy (PFM) measurements (*Materials and Methods*) further confirm this tetragonal structure, with x = 0 films showing typical four-variant, in-plane domain structures and x = 0.2 films showing no in-plane contrast (*SI Appendix*, Figs. S9 and S10 and section S4) as expected for tetragonal symmetry.

Density-functional theory (DFT) calculations (*Materials and Methods*), done using the experimental lattice parameters, were used to explore the structural evolution with $BaTiO_3$ alloying. Increasing the $BaTiO_3$ content tends to stabilize the tetragonal-like structure with the polarization being systematically rotated toward the [001] and the octahedral rotation angles being reduced toward zero (in contrast to the parent $R3c$-like structure with the polarization closer to the [111] and larger octahedral rotation angles; *SI Appendix*, Fig. S11 and section S5. By contrast, for bulk $(1–x)BiFeO_3–(x)BaTiO_3$, the $R3c$-like phase is always preferred across the range of x studied herein. Additionally, excellent agreement between the DFT and the HAADF-STEM results (Fig. 1 *F–H*) is found for $x > 0.2$ compounds; wherein both approaches reveal large out-of-plane cation displacements, small in-plane cation displacements, and reduced octahedral-tilt angles (*SI Appendix*, Fig. S11*F* and section S5). As such, both the experiments and theory provide evidence of stabilization of a tetragonal

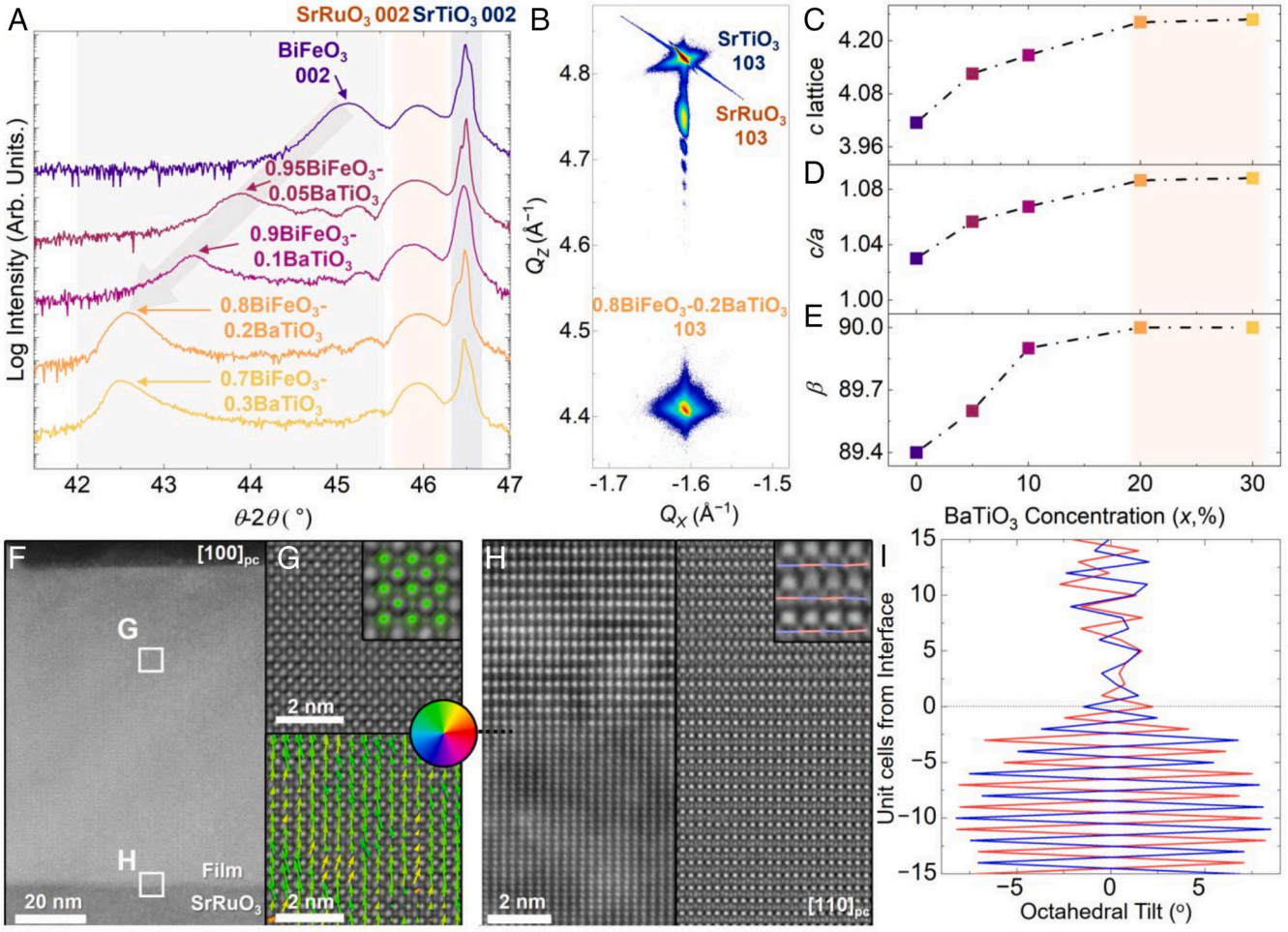

Fig. 1. Strain and chemistry change the structure of $BiFeO_3$ films (*A*) X-ray diffraction patterns of (1−*x*)$BiFeO_3$–(*x*)$BaTiO_3$ (*x* = 0, 0.05, 0.1, 0.2, and 0.3) thin films deposited on $SrRuO_3$/$SrTiO_3$ [001] substrates showing a shift to lower angles of the 002-diffraction condition with increasing *x*. (*B*) X-ray reciprocal space mapping studies about the 103-diffraction condition show the *x* = 0.2 films are fully strained to the $SrTiO_3$ substrate. The evolution of the (*C*) out-of-plane lattice parameter, (*D*) the *c*/*a* lattice parameter ratio or tetragonality, and (*E*), the *β* angle as a function of *x*. For *x* = 0.2 films grown on $SrRuO_3$/$SrTiO_3$ [001], (*F*) wide area, cross-sectional STEM image including (*G*) zoom-in iDPC image showing the atomic positions and local polar displacement mapping revealing out-of-plane aligned polarization, with the *Inset* highlighting local cation vs. anion octahedra polar displacements. From simultaneously obtained (*H*) ADF and iDPC images at the film–$SrRuO_3$ interface along the [110] pseudocubic projection, with the *Inset* highlighting tilting/rotation of the oxygen positions illustrated by the red and blue markings (*I*) the tilting of the oxygen octahedra is measured wherein the blue and red lines show averages of alternating unit cells, with the tilts decreasing to near zero in the *x* = 0.2 films.

phase which is distinct from the phases previously reported in $BiFeO_3$-based films.

Enhanced Ferroelectric Polarization. Having established the stabilization of a distinct tetragonal structure, it is important to explore how the physical properties evolve. First, the leakage of the films decreases with increasing $BaTiO_3$ content (*SI Appendix*, Fig. S12), likely due to the decreased oxygen-vacancy concentration in aliovalent-alloyed $BiFeO_3$ (27, 28) thus addressing one challenge for $BiFeO_3$ (i.e., films can be leaky). Likewise, as the $BaTiO_3$ content is increased, the dielectric constant and loss (Fig. 2*A*), tunability, and temperature dependence of the dielectric constant (*SI Appendix*, Fig. S13) all decrease. The reduced loss and susceptibility are consistent with the improved leakage and the changes in the polarization, respectively (Fig. 2*B*). Polarization-electric field hysteresis loops (*Materials and Methods*) for the *x* = 0 films exhibit saturation polarization (P_s) and coercive field (E_c) values ≈ 68 μC cm^{-2} and ≈ 214 kV cm^{-1}, respectively; in good agreement with previous studies (29). $BaTiO_3$ alloying increases the E_c (≈ 816 kV cm^{-1} for *x* = 0.2 films, respectively) while the P_s first increases (≈ 120 μC cm^{-2} for *x* = 0.1 films) and then decreases. Further increasing the $BaTiO_3$ content to *x* = 0.3 leads to a rather sharp decrease in the dielectric constant and P_s values (≈ 53 μC cm^{-2}) and, as such, most of the remaining discussion focuses on *x* < 0.3 films. This evolution can be understood by considering the changes in polarization and switching mechanisms accompanying the structural evolution. First, in the *x* = 0.1 films, the addition of $BaTiO_3$ drives the system toward a more tetragonal structure with a corresponding polarization rotation from along the [111] toward the [001], resulting in a larger P_s projected onto the out-of-plane direction as compared to the *x* = 0 films. In the *x* = 0.2 films, this polarization rotation to the [001] is complete, but the addition of more $BaTiO_3$ (which has a relatively lower polarization of ≈ 26 μC cm^{-2} in the bulk) leads to a reduction of the overall P_s (also seen in the *x* = 0.3 films). In turn, the E_c evolution is tied to changes in the available switching pathways. In *x* = 0 films, numerous (relatively) lower-energy ferroelastic (i.e., 71° and 109°) switching events are possible, but as the polarization rotates toward the [001] and the structure becomes more tetragonal, these switching pathways are excluded or become energetically costly such that only ferroelectric 180° switching is possible in the *x* = 0.1 and 0.2 films. Such ferroelectric switching pathways typically involve higher barriers (30–33) and thus require a higher electric field for activation (34). This is confirmed by Merz' law (35) fits to switching for these films where the activation field is increased from ≈ 697 kV cm^{-1} to

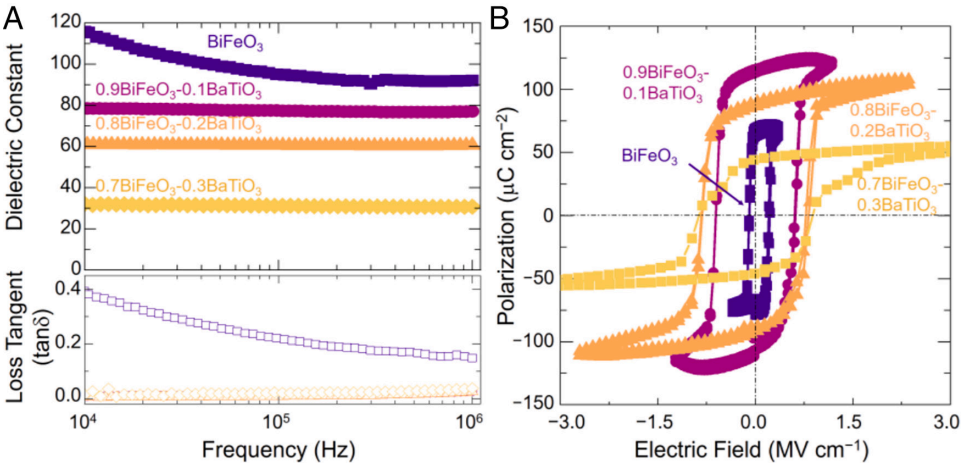

Fig. 2. Evolution of the dielectric and ferroelectric properties. (*A*) Frequency dependence of the dielectric permittivity (*Top*) and loss tangent (*Bottom*) for 25 nm $SrRuO_3$/100 nm $(1-x)BiFeO_3$–$(x)BaTiO_3$ (x = 0, 0.1, 0.2, and 0.3)/25 nm $SrRuO_3$/$SrTiO_3$ [001] heterostructures. (*B*) Polarization-electric field hysteresis loops for the same devices measured at 10 kHz.

≈ 2,435 kV cm^{-1} and to ≈ 3,495 kV cm^{-1} for the x = 0, 0.1, and 0.2 films, respectively (*SI Appendix*, Figs. S14 and S15 and section S7). Thus, the evolution toward a tetragonal structure increases P_s and E_c and enhances the robust ferroelectricity in the system.

Enhanced Ferromagnetic-Like Response. Next, the impact of the strain- and chemistry-induced structural changes on the magnetic order is explored. Room-temperature superconducting quantum interference device (SQUID) magnetometry (*Materials and Methods*) studies reveal intriguing magnetism evolution with $BaTiO_3$ alloying. First, in the out-of-plane direction (*SI Appendix*, Fig. S16*A*), there is minimal difference between films (all <10 emu cm^{-3}). In the in-plane direction (Fig. 3*A*), while the x = 0 films exhibit response consistent with previous results (≈ 3 emu cm^{-3}), the x = 0.2 films show a significantly enhanced saturation magnetization of ≈ 40 emu cm^{-3} with no significant difference observed in the hysteresis loops with in-plane rotation (*SI Appendix*, Fig. S16*B*), implying isotropic magnetic behavior within the plane and perpendicular to the polarization direction. These magnetization values are reproducible across more than 20 films produced by multiple researchers (*SI Appendix*, Fig. S17). The finite ratio of remanent to saturation magnetization (M_r/M_s ≈ 0.5) for the x = 0.2 films also indicates the potential role of magnetic domains in the hysteresis formation. The coercive field (≈ 650 Oe) in the x = 0.2 films is also significantly larger than that in the x = 0 films (≈ 135 Oe), indicating that $BaTiO_3$ alloying induces a harder magnetic character, potentially through the formation of small domains and in contrast to the uniform cycloidal domains in x = 0 films. Further increase of the $BaTiO_3$ concentration in the x = 0.3 films results in the magnetization decreasing relative to that of the x = 0.2 films (*SI Appendix*, Fig. S16*C*). Temperature-dependent measurements reveal that the magnetization is stable up to the upper limit of the operational temperature range of the SQUID magnetometer, but from these data, the temperature of the transition to the paramagnetic phase can be estimated to be in the 400 to 550 K range (*SI Appendix*, Fig. S18 and section S9).

To further confirm the presence of this enhanced magnetization and rule out potential contamination artifacts, angle-dependent X-ray magnetic circular dichroism (XMCD, *Materials and Methods*) measurements were performed at the iron $L_{2,3}$ edges for the x = 0, 0.1, and 0.2 films. These measurements probe the difference in absorption between left and right circularly polarized X-rays and are sensitive to the spin polarization (i.e., ferromagnetic character) of the element being probed. As expected, the x = 0 and 0.1 (*SI Appendix*, Fig. S21) films exhibited no measurable XMCD response, while the x = 0.2 films showed strong circular dichroism at both the $L_{2,3}$ edges (Fig. 3*B*). The dichroism was strongest at low incidence angles and gradually decreased as the beam approaches the surface normal; consistent with the in-plane alignment of magnetization and a robust ferromagnetic-like moment associated with the iron sublattice. The observed compositional evolution of magnetization represents a dramatic change in the magnetic structure of $BiFeO_3$-based films, but its origin is not obvious. To uncover the origins of this magnetic order, a series of comprehensive multimodal studies were conducted, including exchange-bias-heterostructure studies (*Materials and Methods*), angle-dependent, element-specific X-ray magnetic linear dichroism (XMLD, *Materials and Methods*), inelastic-light scattering (*Materials and Methods*), and scanning nitrogen-vacancy (NV) magnetometry (*Materials and Methods*). The results from these studies provided critical insights into the nature of the magnetic order. First, the anisotropy of the tetragonal phase was explored. Prior studies on x = 0 films have established that, in most cases, a preferred mutual orthogonality between the polarization (***P***), antiferromagnetic axis (***L***), and weak ferromagnetic moment (***M***) is expected (36, 37). Indeed, angle-dependent magneto-optic Kerr effect (MOKE) measurements on exchange-coupled $Co_{0.9}Fe_{0.1}/(1-x)BiFeO_3$–$(x)BaTiO_3$ heterostructures (*SI Appendix*, Fig. S22 and section S10) show a strong anisotropy for x = 0 films in both exchange bias (hysteresis-loop shift) and exchange enhancement (coercive field). The solid-solution films, however, show little anisotropy while still maintaining strong exchange enhancement indicating some degree of coupling but little orientational preference. This (an)isotropy is further explored with angle-dependent XMLD studies at the iron $L_{2,3}$ edges. While linear dichroism in $BiFeO_3$ arises from both magnetic and crystal-field effects, the room-temperature response is predominantly of magnetic origin (38, 39). Specifically, the asymmetric intensity between split L_2 peaks arises due to an exchange field acting on the 3*d* spins and depends on the relative orientation of the X-ray polarization vector and the magnetic ordering (40). Thus, the relative intensities of the two peaks as a function of incidence angle can be used to ascertain the direction of ***L***. The intensity ratio between the multiplet peaks L_{2A}/L_{2B} was calculated from X-ray absorption spectroscopy (XAS) (*SI Appendix*, Fig. S23 *A–D*) and plotted as a function of incidence angle (θ) and rotation about the [001] (ϕ). While the L_{2A}/L_{2B} ratio exhibits a strong peak at θ = 90° for all films, indicating a preference for in-plane alignment, there is minimal change in response as a function of ϕ for x = 0.1 and 0.2 films, indicating a relatively weak orientation preference within the plane, consistent with the exchange-interaction measurements (*SI Appendix*, Fig. S23 *E–H*). Thus, the addition of $BaTiO_3$ and the accompanying structural evolution maintains the in-plane orientation of magnetic moments perpendicular to the out-of-plane oriented ***P***, but significantly reduces its orientation preference within that plane, reflecting how

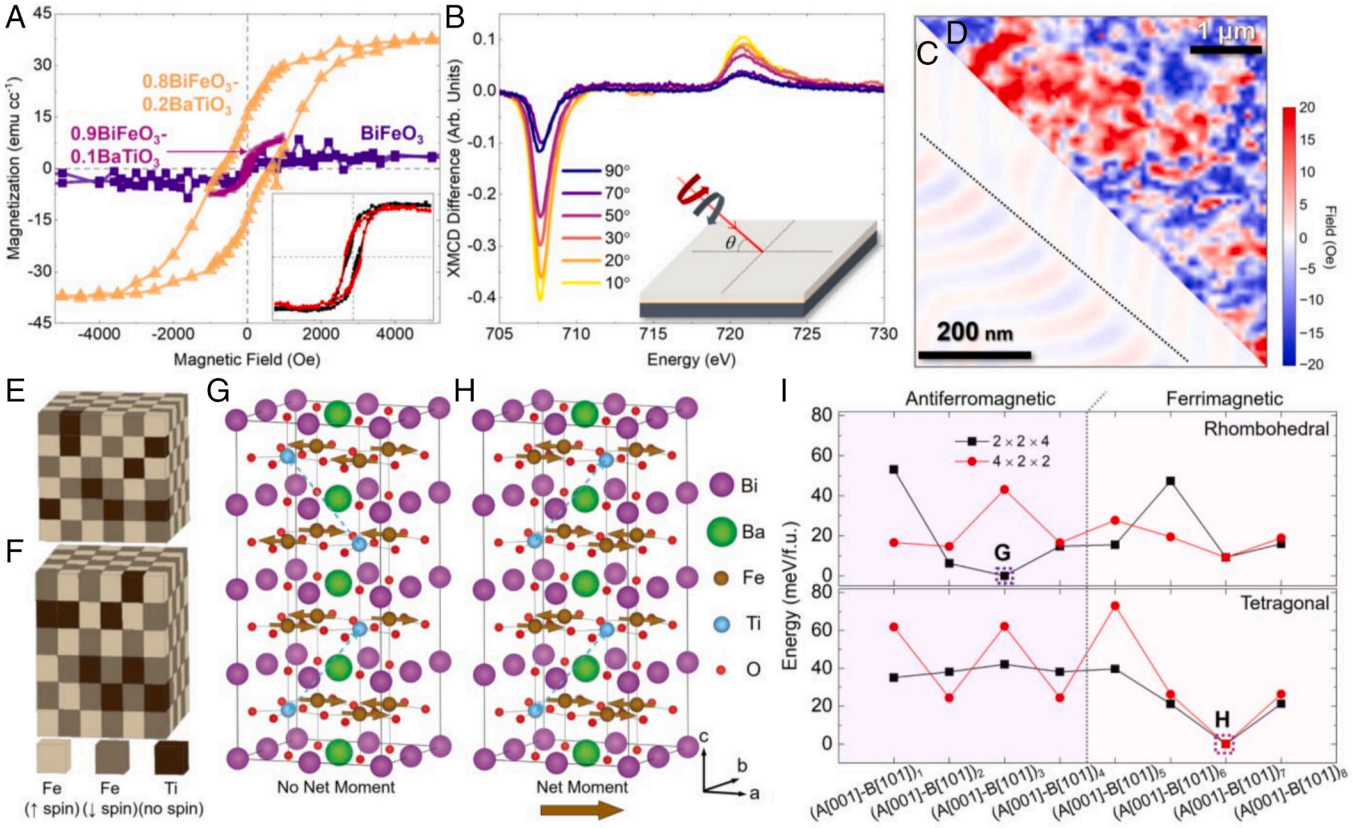

Fig. 3. Magnetism in $(1-x)BiFeO_3$–$(x)BaTiO_3$ (x = 0, 0.1, and 0.2) films. (*A*) In-plane magnetization-magnetic field hysteresis loops measured at 300 K via SQUID magnetometry revealing an enhancement of the magnetization for x = 0.2 films. (*B*) Angle-dependent XMCD difference spectra taken at the iron $L_{2,3}$ edges corroborate the larger magnetization and the preference for in-plane alignment. The arrow indicates the *Right* (blue) and *Left* (red) circularly polarized light. The possible origin of ferromagnetic-like response was confirmed via Scanning-NV magnetometry images corresponding to the (*C*) x = 0 and (*D*) x = 0.2 films wherein the former shows weak contrast consistent with the spin cycloid and the latter shows strong contrast consistent with robust magnetization. The dashed lines demarcate the location of a ferroelectric domain wall. Schematic illustration of (*E*) the rhombohedral structure with random substitution of titanium atoms at the spin-up and spin-down states, preserving the balance between up and down spins and the antiferromagnetic state of $BiFeO_3$ and (*F*) the tetragonal structure with titanium atoms showing a mixture of random substitution and ordered substitution along the [101] at the spin-up and -down states, leading to slight excess of down spins and ferrimagnetism in the solid-solution films. (*G–I*) Calculated energies of the different titanium arrangements along the face diagonal (i.e., [101]) for 80-atom supercells, considering both bulk-like rhombohedral (*Top* row in Fig.1*I*) and tetragonal (*Bottom* row in Fig.1*I*) structures for x = 0.25 films, revealing that the lowest energy state is antiferromagnetic (*G*) in the former and ferrimagnetic in the latter (*H*).

the compositional and structural evolution driven by $BaTiO_3$ alters the magnetic symmetry and order in these films.

How then does this reduction in anisotropy enable a large remanent magnetic moment? One possibility is through the formation of domains, the presence of which was probed by scanning-NV magnetometry (quantitatively and spatially). This method is sensitive to small (< 5G) stray magnetic fields at the nanoscale (41). For comparison, measurements were performed for an x = 0 film deposited on a $DyScO_3$ [110] substrate (Fig. 3*C*) and for an x = 0.2 film deposited on a $SrTiO_3$ substrate (Fig. 3*D*). As reported previously (42), x = 0 films on $DyScO_3$ substrates exhibit a periodic chevron-like pattern generated by the interaction of the spin cycloid with the ferroelectric domain walls (43). By contrast, the x = 0.2 films show no fine structure but ≈ 10-times larger stray magnetic fields, consistent with the larger observed magnetic moment. This is indicative of disordered magnetization, where the system consists of many small, highly magnetized domains.

Another question then remains, why is the observed moment so large? Inelastic light scattering (ILS) results for x = 0, 0.1, and 0.2 films indicate that the magnon structure remains relatively unchanged with the addition of $BaTiO_3$ (*SI Appendix*, Fig. S24 and section S11). Compared to the relatively small canting angle of $BiFeO_3$ (≈ 1°), a significantly larger canting approaching 5° would be necessary to produce the observed moment in the x = 0.2 films; however, first-principles calculations predict the spin-canting angle to be 0.6° for the x = 0.2 films, suggesting that a 5° increase would be highly energetically unfavorable. Instead, a mechanism is proposed based on DFT calculations that show that specific types of local, short-range ordering of nonmagnetic titanium on iron sites could produce net moments of a ferrimagnetic nature (*SI Appendix*, section S12). Here, the shorthand A[hkl]-B[h'k'l'] denotes ordering of A-site (Bi/Ba) and B-site (Fe/Ti) cations along the specified crystallographic directions [hkl] and [h'k'l']. If the titanium substitution is random (Fig. 3*E*), no net moment is expected. If the titanium-cation distribution is, however, nonrandom or (partially) ordered such that unequal numbers of spin-up and -down iron sites are replaced (Fig. 3*F*), this can produce a strong net moment on a local scale due to the high moments of the iron cations. To probe this concept, the energetics of cation orderings were explored in 2 × 2 × 2 supercells (six iron and two titanium sites) of both the rhombohedral (bulk-like) and tetragonal phases (using the experimentally determined lattice parameters) for x = 0.25 films (*SI Appendix*, Fig. S25). Only arrangements of titanium cations along the [101] and [110] lead to ferrimagnetic states with a net moment (estimated magnetization ≈ 192 emu cm^{-3}). It is found that the antiferromagnetic arrangements have the lowest energy for both rhombohedral and tetragonal structures; however, the energy preference for the antiferromagnetic arrangements is two times smaller in the tetragonal structure and is, overall, quite small (≈ 10 meV $f.u.^{-1}$) (*SI Appendix*, Fig. S26). The ratio of the number of low-energy

antiferromagnetic to ferrimagnetic arrangements is ≈ 2:1, and if all low-energy antiferromagnetic and ferrimagnetic 2 × 2 × 2 cell arrangements are equally likely, approximately one-third of the local titanium arrangements will be ferrimagnetic; resulting in a net moment ≈ 64 emu cm^{-3} (reasonably close to the measured value of ≈ 40 emu cm^{-3}). To further examine whether a preference for the ordered structure of titanium can result in the observed magnetism, larger 4 × 2 × 2 and 2 × 2 × 4 supercell calculations were performed for the low-energy ferrimagnetic $A_{[001]}$-$B_{[101]}$ 2 × 2 × 2 cells (*SI Appendix*, Figs. S27 and S28) stacked so as to produce antiferromagnetic (Fig. 3*G*) and ferrimagnetic (Fig. 3*H*) supercells (*SI Appendix*, Fig. S29). In the rhombohedral structure, the lowest energy orderings for the $A_{[001]}$-$B_{[101]}$ stackings are antiferromagnetic (*Top* row, Fig. 3*I*), while in the tetragonal structure the lowest energy orderings are ferrimagnetic (*Bottom* row, Fig. 3*I*). Calculations for even larger (4 × 2 × 4) supercells further confirm these results (*SI Appendix*, Fig. S30). Furthermore, calculations for the model ferrimagnetic structure based on the DFT-estimated exchange-coupling parameters and mean-field theory (*SI Appendix*, section S9) suggest a transition temperature to the paramagnetic state to be ≈ 537 K; this is consistent with experimental observations, considering the expected ~100 K overestimation of the transition temperature by mean-field theory (*SI Appendix*, section S9). Therefore, the experimentally observed ferromagnetic-like behavior of the $BaTiO_3$-alloyed films is assigned to a ferrimagnetism mechanism resulting from the low energy of local, short-range titanium alignment along the [101] which is made possible by the tetragonal distortion of the $x = 0.2$ films.

The randomly distributed, large magnetic moments observed in scanning-NV magnetometry could be related to regions of local titanium ordering. The interaction between these magnetic regions could then be mediated by exchange with the broader antiferromagnetic lattice, giving reason to expect similar symmetries to those of L as well as providing a potential reason for a remanent, rather than superparamagnetic-like magnetization—akin to how elastic energy in relaxor ferroelectrics stabilizes local polar regions, preventing them from reorienting freely and thereby contributing to a remanent polarization. Similar mechanisms have previously been proposed in chemically disordered oxide systems (44), resulting in a net, spin-glass-like magnetization. Such locally ordered titanium arrangements should also be controlled by the deposition conditions, and this is supported by the fact that the magnetic behavior of $x = 0.2$ films is dependent on the growth temperature and laser fluence (*SI Appendix*, Figs. S31–S33 and section S13). Taken together, these results indicate that the robust magnetic behavior arises from a nuanced mechanism which may potentially be exploited to achieve improved multiferroic properties in other systems.

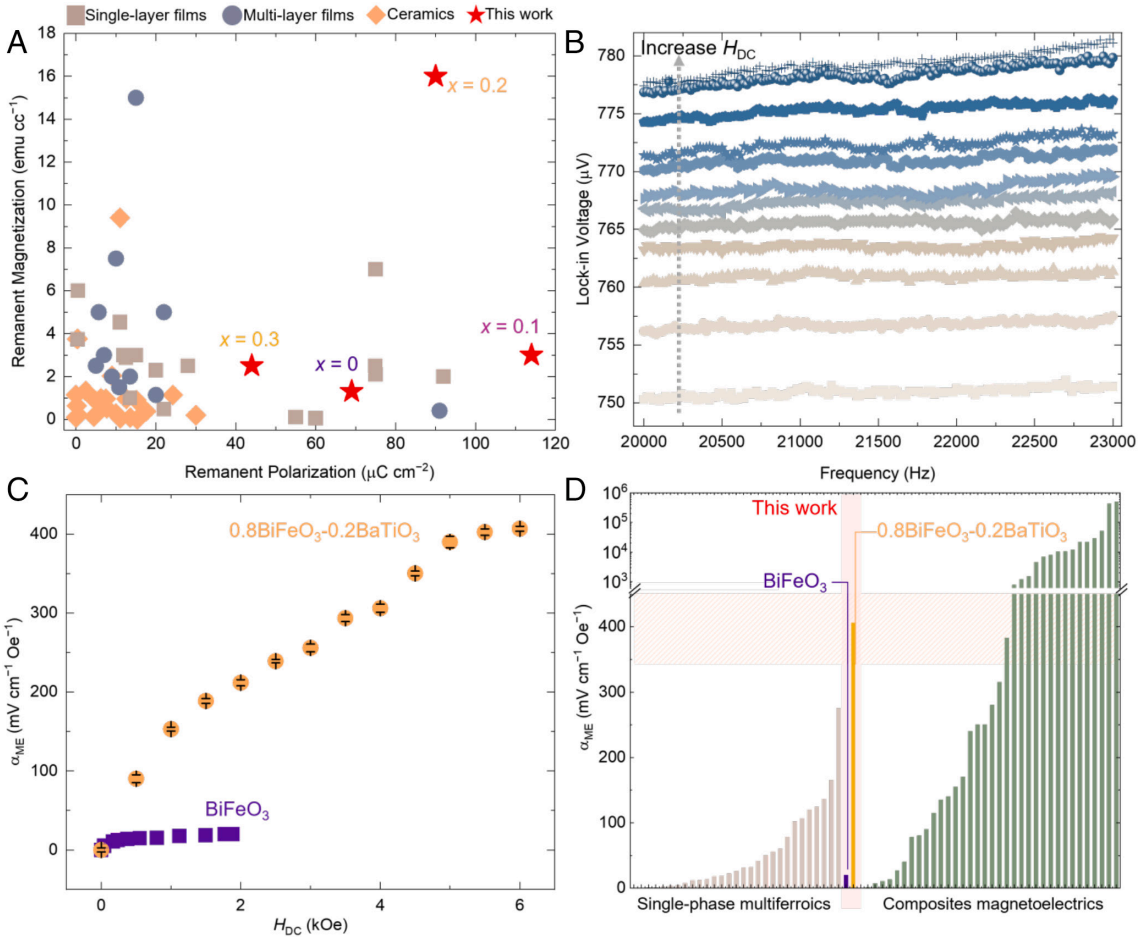

Fig. 4. Summary of ferroelectric, magnetization, and magnetoelectric coupling (*A*) the graph summarizes the remnant polarization and remnant magnetization of various multiferroic materials (*SI Appendix*, Table S1). (*B*) The evolution of magnetoelectric coupling, α_{ME} values are extracted from the raw data from a lock-in with increasing the H_{DC} for both the $BiFeO_3$ (*SI Appendix*, section S13) and 0.8$BiFeO_3$–0.2$BaTiO_3$. The data shows a frequency sweep from 20 to 23 kHz with H_{AC} = 7 Oe (*C*) Experimentally determined linear magnetoelectric coefficient α_{ME}, for the 100-nm-thick epitaxial 0.8$BiFeO_3$–0.2$BaTiO_3$, as compared with end member $BiFeO_3$ films, plotted as a function of applied bias magnetic field. The measured α_{ME} in the single-phase solid-solution large remnant polarization and magnetization epitaxial film is more than an order of magnitude higher than that for the end member. (*D*) The magnetoelectric voltage coefficient α_{ME} in numerous multiferroic materials including both single-phase multiferroics and composite magnetoelectrics (*SI Appendix*, Table S2).

Robust Polarization, Magnetization, and Magnetoelectric Coupling. Thus far, this work has demonstrated large polarization and magnetization in $BaTiO_3$-alloyed films. The importance of this observation is made evident through a review of previous work on single-phase multiferroic materials (Fig. 4*A* and *SI Appendix*, Table S1). Historically, it has been challenging to achieve simultaneous large room-temperature polarization and magnetization in a single material, but in the x = 0.2 films, significant improvement of both properties has been achieved. While interesting, the real impact lies in the potential for enhanced magnetoelectric coupling between the polar and magnetic orders. Therefore, magnetoelectric-coupling measurements (*Materials and Methods*) were carried out on x = 0 (*SI Appendix*, Fig. S35 and section S14) and x = 0.2 (Fig. 4*B*) films and used to extract the magnetoelectric-voltage coefficient α_{ME} (Fig. 4*C*). These measurements reveal that the α_{ME} for the x = 0.2 films is as large as ≈ 400 mV cm^{-1} Oe^{-1} (at an applied field of 6 kOe); a value which is nearly two orders of magnitude higher than that measured for the x = 0 films. Furthermore, the x = 0 films saturate at lower fields (≈ 0.35 kOe) as compared to the x = 0.2 films (≈ 5.5 kOe); these results are consistent with the magnetization-magnetic field hysteresis loops (Fig. 3*A*). Thus, by increasing the magnitude of both the magnetization and polarization in a $BiFeO_3$-based material, a large α_{ME} is obtained which is competitive with values that have previously only been achieved in composite magnetoelectrics (Fig. 4*D* and *SI Appendix*, Table S2).

Discussion

This work demonstrates the stabilization of a tetragonal phase distinct from the previously reported super-tetragonal phase in $(1-x)BiFeO_3$–$(x)BaTiO_3$ (x = 0.2 and 0.3) films which exhibits robust simultaneous ferroelectric and ferrimagnetic order. Using a suite of advanced structural, dielectric/ferroelectric, and (anti) ferromagnetic characterization techniques in conjunction with high-resolution STEM and first-principles calculations, an in-depth understanding of the connection between structure, chemistry, and properties and a mechanism (based on ferrimagnetism from local, short-range ordering of titanium cations) for the evolution of the observed magnetic properties has been presented. The concepts put forth in this work could spark the discovery of new materials and phenomena beyond this system. In turn, looking toward potential applications, the realization of a single-phase multiferroic could enable more facile introduction of such materials into devices—especially those required to function in miniaturized devices for which thin-film structures of a single material are required (45).

Materials and Methods

Thin-Film Growth and Target Preparation. The 10 to 100 nm $(1-x)BiFeO_3$–$(x)BaTiO_3$ (x = 0, 0.05, 0.1, 0.2, and 0.3)/30 nm $SrRuO_3$ heterostructures were grown on $SrTiO_3$ [001], $DyScO_3$ [110], and $GdScO_3$ [110] substrates by pulsed-laser deposition using a KrF excimer laser (wavelength 248 nm; LPX 300, Coherent). The substrate was cleaned by sonicating in acetone and then isopropyl alcohol for 10 min each. The substrates were attached to a resistive Inconel heater using colloidal silver paint and heated up to 80°C to cure the silver paint by removing the solvent. The chamber base pressure below 1 × 10^{-5} Torr. After reaching sufficient base pressure, the system was set to a dynamic oxygen partial pressure of 200 mTorr for heating. During heating to the growth temperatures, the targets were preablated with 2,000 pulses at 15 Hz with a shutter in front of substrates to establish a uniform surface and remove unwanted adsorbates from ground targets. The $SrRuO_3$ layer was deposited from a commercially prepared ceramic target (Praxair Surface Technologies) at a heater temperature of 680 °C in a dynamic oxygen partial pressure of 200 mTorr, laser fluence of 1.0 J cm^{-2}, laser repetition frequency of 15 Hz, and an on-axis target-to-substrate distance of 57 mm. The $BiFeO_3$ films were deposited from commercially prepared ceramic targets (Praxair Surface Technologies) with composition $Bi_{1.1}FeO_3$ to compensate for evaporative loss of bismuth during the growth. These films were grown at 700 °C in a dynamic oxygen partial pressure of 100 mTorr at a laser fluence of 1.1 J cm^{-2}, a laser repetition frequency of 20 Hz, and an on-axis target-to-substrate distance of 57 mm. The $(1-x)BiFeO_3$–$(x)BaTiO_3$ (x = 0.1, 0.2, and 0.3) films were grown from solid-solution $(1-x)BiFeO_3$–$(x)BaTiO_3$ targets produced by the team. The targets were prepared by conventional solid-state synthesis. Analytical grade starting powders of Bi_2O_3, TiO_2, Fe_2O_3, and $BaCO_3$ were weighed stoichiometrically with 10% at. excess Bi_2O_3 and mixed by ball milling. The mixtures were calcined at 675°C for 12 h. After ball milling for 12 h, the calcined powders were pressed into one-inch-diameter pellets in a uniaxial press, surrounded by sacrificial powder of the same composition, and then sintered at temperatures between 900°C and 950°C, depending on the specific composition, for 2 h. Subsequent growth of films was done at 710°C in a dynamic oxygen partial pressure of 20 mTorr at a laser fluence of 0.71 J cm^{-2}, a laser repetition frequency of 20 Hz, and an on-axis target-to-substrate distance of 57 mm. After deposition, the samples were cooled to room temperature at a rate of 10°C min^{-1} in a static ~700 Torr partial pressure of oxygen.

X-Ray Diffraction. To study the crystal structure of each film (x = 0, 0.1, 0.2, and 0.3), symmetric θ-2θ linescans and reciprocal spacing mapping (RSM) studies were completed with a X'Pert 3 MRD diffractometer (Malvern PANalytical) equipped with a 1.8 kW copper X-ray source and hybrid optic monochromator (with a Bragg–Brentano mirror and a germanium two-bounce monochromator) which provides monochromatic K_α radiation (wavelength of 1.5406 Å). 1/2° and 1/16° divergence slits were placed on the incident optics side for linescans and RSMs, respectively. The diffracted X-rays were collected on a PIXcel3D detector. Linescans were conducted in the Bragg–Brentano geometry with 0.01° step size and a count time of 0.4 s per step. The detector was set to 0D mode with an active length of 0.275 mm. Asymmetric RSMs were measured using a frame-based 1D detector mode with a 0.005° step size and 2,500 s per step counting time. The crystalline quality of all films (x = 0, 0.1, 0.2, and 0.3) were confirmed using X-ray rocking curves about the 002_{pc}-diffraction condition of each film.

Scanning Transmission Electron Microscopy (STEM). Samples for STEM imaging were prepared by mechanical wedge polishing followed by ion milling to electron transparency with a Fischione 1051 TEM mill. STEM datasets were acquired on a probe-aberration-corrected Thermo Fisher Scientific Themis Z S/TEM using an accelerating voltage of 200 kV, probe convergence angle of 18.8 mrad, and probe current of 30 pA. STEM HAADF, ADF, and iDPC images were acquired with collection angles of 63 to 200 mrad, 25 to 152 mrad, and 6 to 24 mrad, respectively. To account for specimen drift, image series were registered using nonrigid registration using parameters optimized for STEM (46). A custom Python-based Gaussian atom column fitting and analysis script was used to compare atom column normalized intensities, cation–cation distances, and cation vs. anion displacements. To better understand the coupling of oxygen octahedral tilts across the electrode–film interface, ADF and iDPC images from across the interface of x = 0.1 and 0.2 films were examined along the [110]-pseudocubic projection [100] direction of orthorhombic $SrRuO_3$ and analyzed using the above procedures (*SI Appendix*, Fig. S4). Energy dispersive X-ray spectroscopy was performed using Super X detectors with a probe current of 200 pA and quantified in the Thermo Fisher Scientific Velox software.

Piezoresponse Force Microscopy (PFM). Dual AC resonance tracking (DART)-PFM was performed on a commercial MFP-3D atomic force microscope (AFM, Asylum Research) for 100 nm $(1-x)BiFeO_3$–$(x)BaTiO_3$ (x = 0, 0.1, and 0.2)/30 nm $SrRuO_3/SrTiO_3$ [001] heterostructures. The PFM scans were obtained using a titanium/iridium-coated silicon cantilever (Olympus Electrilever) with a nominal tip radius of < 25 nm. To confirm the domain switching of the x = 0, 0.1, and 0.2 films, the samples were poled in a box-in-box pattern by DC bias applied through the tip. First, a negative switching voltage was applied to a 5 × 5 μm area. Then, within that area, a positive voltage was applied in a 3 × 3 μm area to switch the film in the opposite direction. ±6 V was used for x = 0 films and ±10 V was used for solid-solution films. Scans were conducted at 0 and 45° to compare in-plane responses.

Electrical, Dielectric, and Ferroelectric Characterization. All (di-)electrical properties were measured on 30 nm $SrRuO_3$/100 nm $(1-x)BiFeO_3$–$(x)BaTiO_3$ (x = 0, 0.1, 0.2, and 0.3)/30 nm $SrRuO_3/SrTiO_3$ [001] heterostructures. Circular

capacitors 25 μm in diameter were patterned via photolithography and produced by ion milling through the top electrode (Intlvac Nanoquest, Beam voltage: 500 V, Beam Current 38 mA, Accelerator: 100 V). The photolithography was conducted in the following steps. After sonicating the sample using acetone (5 min) and isopropyl alcohol (5 min), photoresist (OCG 825 35CS) was coated on the film using the spin coater (10 s at 1,000 rpm and 30 s at 9,000 rpm). The samples were then placed on a glass slide and baked for 1 min on the hot plate at 95 °C. A mask was then placed on the film and exposed to ultraviolet light (395 nm) for 5 s. The sample was then soaked in Microposit developer concentrate diluted with DI water in a 1:1 volume ratio for 30 s and then stirred vigorously in DI water for 10 s. After milling, the photoresist was removed by sonicating in acetone.

The leakage current as a function of electric field was measured with unswitched triangular mode using a Precision Multiferroic Tester (Radiant Technologies, Inc.) at room temperature. Dielectric constant and loss tangent were measured as function of DC electric field ($\pm$2 MV cm^{-1}) and frequency (10 kHz to 1 MHz). Measurements up to a maximum AC field strength of 10 to 50 kV cm^{-1} were conducted using an E4990A Impedance Analyzer (Keysight Technologies) at room temperature. The ferroelectric polarization was probed with a double bipolar triangular waveform of a given amplitude (up to $\pm$3 MV cm^{-1}) and frequency (20 kHz) using a Precision Multiferroic Tester (Radiant Technologies, Inc.) at room temperature.

XAS, XMLD, and XMCD. These X-ray spectroscopy measurements were performed on $x = 0$, 0.1, and 0.2 films at beamline 4.0.2 of the Advanced Light Source at Lawrence Berkeley National Laboratory. All XAS spectra were obtained in the total electron yield geometry, wherein the samples were mounted on a copper rod and electrically connected using carbon tape and silver paint. The background signal was simultaneously collected and divided out from the overall signal. The spectra were then normalized for comparison. For the XMLD measurements, an azimuthal sample holder was used, such that the samples could be rotated arbitrarily. Each measurement was repeated at least four times with two linear X-ray polarizations which are mutually orthogonal to each other and the incident X-ray direction. Only data from a single polarization were used to extract angle-dependent L_2 peak ratios, while both were used to calculate linear dichroism. XMCD measurements were performed at the iron $L_{2,3}$ edges under a $\pm$0.4 T magnetic field using circularly polarized light, with dichroism obtained from average differences between opposite polarization and field configurations. Specifically, the normalized X-ray absorption spectra under right circularly polarized light/positive field and left circularly polarized light/negative field were averaged together and subtracted from the average, normalized spectra under right circularly polarized light/negative field and left circularly polarized light/positive field. Magnetic hysteresis loops for the $x = 0.2$ film were measured at the energy of maximum dichroism over $\pm$0.4 T, and angle-dependent measurements (from 10° to 90°) were used to probe magnetic anisotropy.

SQUID Magnetometry. A magnetic property measurement system (MPMS-XL, Quantum Design) equipped with DC scan option (DC refers to the dc magnetic field) was used to measure the magnetization of $x = 0$, 0.1, and 0.2 films. In DC scanning, a sample moves linearly over several centimeters through second-order gradiometer detection coils, which induces a SQUID voltage as a function of the sample-position curve. The magnetic moment of the sample is derived from regression fits of the induced voltage curve to a single dipole response function. For regression fitting (to obtain single data in the output), 32 data points with scan length of 4 cm and 2 scan-averaging were used for better accuracy. All magnetization hysteresis measurements were completed at 300 K. The data were collected in a magnetic field up to 2 T. For better accuracy, the data were collected in the no-overshoot field mode where the magnetic field was stabilized for 120 s before the measurements. The raw data were corrected to account for the diamagnetic (background) contributions from the substrates using the high field data (via a linear fit). The sample size was accurately measured using a microscope to extract the volume of the film. The film thicknesses are 70 nm, 75 nm, 95 nm, 95 nm, and 100 nm for the laser-fluence-dependent samples grown at 0.53 J cm^{-2}, 0.62 J cm^{-2}, 0.71 J cm^{-2}, 0.79 J cm^{-2}, and 0.88 J cm^{-2}, respectively. As an internal check, magnetization hysteresis was also verified using the substrate centering at 1 T magnetic field. The final data appear to be identical to the hysteresis measured by centering using film magnetic volume at low field of 0.05 T. To understand the temperature-dependent behavior, the magnetization of the $x = 0$ and 0.2 heterostructures were measured as a function of the temperature at a magnetic field of 120 Oe ($x = 0$ films) and 3,000 Oe ($x = 0.2$ films) after being field cooled to low temperatures under an applied field of 10,000 Oe (*SI Appendix*, section S9). The data were recorded upon warming from 2 to 400 K. The magnetic field values used in these measurements correspond to those that produce the largest moments in the magnetic hysteresis loops of the films.

Scanning-NV Magnetometry. To observe a real-space picture of the magnetization, scanning-NV magnetometry was performed on a Qnami ProteusQ, based on the general scheme outlined previously (47, 48). Parabolic diamond tips hosting a single NV center (Quantilever MX+) were used to acquire the data. $BiFeO_3$ deposited on $DyScO_3$ was used as a control and $x = 0.2$ films was measured at multiple length scales to confirm the absence of fine structure. Samples were measured in a ~20 G static background field. All measurements were done at room temperature.

Magneto-optic Kerr effect: Exchange-Interaction Studies. To probe the evolution of the exchange interactions with $BaTiO_3$ alloying, 3 nm Pt (as a capping layer)/2.5 nm $Co_{0.9}Fe_{0.1}$ films were deposited using DC sputtering at argon partial pressures of 7 mTorr and 2.5 mTorr, respectively, at room temperature under a static magnetic field (200 Oe) along the in-plane [100] on bare $SrTiO_3$ [001] substrates as well as $x = 0$, 0.1, and 0.2 films. Subsequent magnetic properties were obtained using MOKE measurements which were performed in the longitudinal geometry, with the polarization of light (5 mW) parallel to the change in magnetization. A two-pole electromagnet and a rotational stage were used to control the direction of the in-plane magnetic field with respect to the sample. Quarter-waveplates and polarization filters were used to maximize the MOKE signal at the photodiode.

Magnetoelectric Coupling. Coupling between ferroic orders in a material can produce a magnetoelectric effect (charge generation resultant from an applied AC magnetic field), a phenomenon that has been well established to exist in the single phase multiferroic $BiFeO_3$ thin films (29). The magnetoelectric-voltage coefficient $\alpha_{ME} = V/(t \times H_{AC})$, where V is the induced voltage and t is the thickness of the film and is typically expressed in units of electric field per unit magnetic field (e.g., V cm^{-1} Oe^{-1}). The α_{ME} directly relates the induced electric field (or voltage which can readily be probed with a lock-in amplifier) to the applied magnetic field. As such, direct measurements of α_{ME} were completed for $(1-x)BiFeO_3$-$(x)BaTiO_3$ ($x = 0$ and 0.2) heterostructures using established procedures (49, 50). In brief, the heterostructures were mounted in a transverse configuration (i.e., with AC magnetic field (H_{AC}) and DC magnetic field (H_{DC}) applied in-plane and electric field measured through the film thickness; *SI Appendix*, section S14). The top and bottom electrodes of the capacitor devices were connected to the input of a lock-in amplifier to measure the resulting voltage being generated by the sample as H_{AC} (with peak-to-peak amplitude of 7 Oe) was applied at various H_{DC} (0 to 6 kOe). H_{AC} was generated via a pair of Helmholtz coils driven using the output signal of the lock-in amplifier at 20 kHz, and the magnitude of H_{AC} was subsequently scaled up using a bipolar power amplifier. The magnetoelectrically generated voltages for the $0.8BiFeO_3$–$0.2BaTiO_3$ heterostructures and parent $BiFeO_3$ heterostructures were measured using a lock-in amplifier (Ametek/Signal Recovery 7280). Typical raw data (Fig. 4*B* and *SI Appendix*, section S14), here showing a frequency sweep from 20 to 23 kHz (51, 52) with $H_{AC} = 7$ Oe at various static bias H_{DC} fields), reveal increasing lock-in voltage with increasing magnetic field and suggest that there is coupling between the magnetic and polarization order parameters.

First-Principles DFT Calculations. Spin-polarized DFT calculations were performed using the plane wave basis set as implemented in the Quantum-Espresso simulation package. The nucleus and core electrons were represented by Vanderbilt ultrasoft-pseudopotentials taken from the GBRV database (53). The exchange-correlation energy was approximated by the Perdew–Burke–Ernzerhof Generalized Gradient Approximation (GGA) functional for solids (PBEsol). The kinetic-energy cutoff of the plane-wave basis set was 50 Ry. The structures were relaxed until the forces on every atom were $\leq 10^{-3}$ a.u. The effect of strong electron–electron correlation at the iron sites was considered by performing GGA + U calculations in which a Hubbard-like term is added to the effective potential for a better treatment of the local correlation effects for strongly correlated 3*d* electrons of iron. Following previous work (54), we use the approach of Dudarev et al. (55) in which an effective Hubbard U parameter (U_{eff}) is added to the Hamiltonian. U_{eff} is defined by $U_{eff} = U - J$ where U is the Hubbard parameter and J is the exchange interaction.

To calculate the magnetic moment of the iron atoms, we used the Quantum Espresso package and the standard method for atomic magnetic moment evaluation used in previous work on $BiFeO_3$ (54). Here, the up- and down-spin wavefunctions of the occupied orbitals of the final relaxed structure are projected onto the iron *d* orbitals within a certain cut-off radius to obtain magnetic-moment projection values m_{up} and m_{down}. Then, the number of unpaired spins, which gives the magnetic moment on the atom m_{tot}, is calculated according to $m_{tot} = 5\ (m_{up} - m_{down})/(m_{up} + m_{down})$. In our $(1-x)BiFeO_3$–$(x)BaTiO_3$ calculations, we considered the default value of the cut-off radius, and therefore Quantum Espresso will take the cut-off radius defined in the pseudopotential (GBRV) files for each species. The cut-off radius for iron was 1.55 Bohr. We find that the magnetic moment at the iron sites for all the structures of $0.75BiFeO_3$–$0.25BaTiO_3$ considered in this study is $\approx 3.8\ \mu_B$ due to the d^5 electron configuration of Fe^{3+}; consistent with the theoretically calculated magnetic moment at the iron sites for $BiFeO_3$ (54). The lower value of the moment compared to the formal value ($5\ \mu_B$) is due to the hybridization of the *d* electrons with other atoms.

To model the evolution of the relative energetics of the different possible phases of the experimentally grown films with increasing $BaTiO_3$ films, all calculations were performed with the in-plane lattice parameters fixed at the lattice constant of the $SrTiO_3$ substrate ($a = b = 3.90$ Å; consistent with what was observed in the X-ray studies) while the vertical lattice parameter was relaxed. These calculations showed *c*/*a* values that were too small as compared to the experimental results. Therefore, calculations at the experimental lattice parameters were performed to provide a more accurate evaluation of the $(1-x)BiFeO_3$–$(x)BaTiO_3$ heterostructures. A cubic supercell consisting of 40 atoms was used for the study of the solid-solutions because such a 40-atom cubic cell accurately captures the structure and chemical order of the $x = 0$ pseudorhombohedral phase. The Brillouin zone was sampled by a $2 \times 2 \times 2$ Monkhorst-Pack (MP) *k*-point mesh.

For the theoretical calculations of the tetragonal phase of $x = 0.25$ films, the lattice constants were extracted after interpolating the experimental lattice constants at different concentrations ($x = 0.2$ and 0.3) for the films in this work. Additionally, the bulk rhombohedral phase, for which the cubic volume was set to the known experimental volume of the bulk $0.75BiFeO_3$–$0.25BaTiO_3$ *R*-phase (56), was considered. The calculations were carried out using $2 \times 2 \times 2$ supercells, where six *A* (*B*) and two *A* (*B*) sites are occupied by bismuth (iron) and barium (titanium), respectively. Additionally, larger, $4 \times 2 \times 2$, $2 \times 2 \times 4$, and $4 \times 2 \times 4$ 80- and 160-atom supercells were also considered. For the relaxation of ionic position, the Brillouin zone integration was carried out using a $2 \times 2 \times 2$ Monkhorst-Pack k-point mesh for the $2 \times 2 \times 2$, $4 \times 2 \times 2$, $2 \times 2 \times 4$, and $4 \times 2 \times 4$ supercells. For the calculation of final energies, higher-density Monkhorst-Pack $4 \times 4 \times 4$, $2 \times 4 \times 4$, $4 \times 4 \times 2$, $2 \times 4 \times 2$ k-point meshes, respectively, were used (45).

ILS Spectroscopy. ILS spectroscopy was carried out at room temperature (≈300 K) in the backscattering configuration (i.e., $z(x, x)\bar{z}$ and $z(x, y)\bar{z}$, $x \parallel [110]$, $y \parallel [1\bar{1}0]$, $z \perp [001]$), under ≈0.4 mW, 325 nm HeCd laser excitation, focused to an intensity of ≈250 mW mm^{-2} using a microscope objective (Thorlabs, LMUL-50X-UVB). That is, the polarization of incident light was aligned along [110], while scattered light was collected separately parallel, and perpendicular, to [110]. Light was dispersed by a triple monochromator (Horiba Jobin-Yvon, T64000, 2,400 grooves mm^{-1} gratings blazed at 325 nm) and collected with an air-cooled electron-multiplying charged coupled detector (Andor, Newton). The absorption depth of the light was less than 100 nm, thus no scattering from the substrate is apparent in these spectra (*SI Appendix*, section S8).

Data, Materials, and Software Availability. Study data are included in the article and/or *SI Appendix*.

ACKNOWLEDGMENTS. We thank Hossein Taghinejad and James G. Analytis for their support in completing some of the SQUID-based magnetic measurements. T.Y.K., A.P, A.S, J.E.S., I.G., and L.W.M. acknowledge the support of the Army Research Office under Grant W911NF-21-1-0126. J.S. acknowledges the support of the Army Research Office under Grant W911NF-21-1-0118 and the NSF GRFP. M.X., R.R., A.M.R., J.M.L., J.E.S., I.G., and L.W.M. acknowledge that this research was sponsored by the Army Research Laboratory and was accomplished under Cooperative Agreement Number W911NF-24-2-0100. The views and conclusions contained in this document are those of the authors and should not be interpreted as representing the official policies, either expressed or implied, of the Army Research Laboratory or the U.S. Government. The U.S. Government is authorized to reproduce and distribute reprints for Government purposes notwithstanding any copyright notation herein. S.H., I.H., C.K., R.R., and L.W.M. acknowledge additional the support from the U.S. Department of Energy, Office of Science, Office of Basic Energy Sciences, Materials Sciences and Engineering Division under Contract No. DE-AC02-05-CH11231 [Codesign of Ultra-Low-Voltage Beyond CMOS Microelectronics (MicroelecLBLRamesh)] for the development of materials for low-power microelectronics. P.M., R.R., and L.W.M. acknowledge additional support from the Army Research Office Army Research Office under the ETHOS MURI via cooperative agreement W911NF-21-2-0162. D.K. acknowledges support from the National Science Foundation under Grant DMR-2102895. P.S. acknowledges support from the Massachusetts Technology Collaborative, Award number #22032. A.P and I.G. acknowledge additional support from Israel Science Foundation under Grant 1479/21. R.R. and L.W.M. acknowledge additional support from the NSF under Grant DMR-2329111. Computational support for magnetic exchange coupling was provided by the National Energy Research Scientific Computing Center, a U.S. Department of Energy, Office of Science, User Facility located at Lawrence Berkeley National Laboratory. This work made use of the MIT.nano characterization facilities. This research used resources of the Advanced Light Source, which is a DOE Office of Science User Facility under Contract No. DE-AC02-05CH11231.

Author affiliations: [a]Department of Materials Science and NanoEngineering, Rice University, Houston, TX 77005; [b]Rice Advanced Materials Institute, Rice University, Houston, TX 77005; [c]Department of Materials Science and Engineering, University of California, Berkeley, CA 94720; [d]Department of Chemistry, Bar-Ilan University, Ramat Gan 5290002, Israel; [e]Department of Materials Science and Engineering, Massachusetts Institute of Technology, Cambridge, MA 02139; [f]Department of Chemistry, University of Pennsylvania, Philadelphia, PA 19104; [g]Materials Sciences Division, Lawrence Berkeley National Laboratory, Berkeley, CA 94720; [h]Department of Physics, University of California, Berkeley, CA 94720; [i]Materials Science and Technology Division, United States Naval Research Laboratory, Washington, DC 02375; [j]Department of Mechanical Engineering and Mechanics, Drexel University, Philadelphia, PA 19104; [k]Department of Physics, Drexel University, Philadelphia, PA 19104; [l]Department of Materials Science and Engineering, Korea University, Seoul 02841, Republic of Korea; [m]Department of Physics, Northeastern University, Boston, MA 02115; [n]Department of Physics and Astronomy, Rice University, Houston, TX 77005; and [o]Department of Chemistry, Rice University, Houston, TX 77005

Author contributions: T.Y.K. designed research; T.Y.K., J.S., A.P., M.X., A.S., S.H., P.M., I.H., P.F., T.M., M.S., A.J.R., S.M., L.W., T.J.P., D.K., C.K., P.S., and I.G. performed research; T.Y.K., A.P., M.X., A.S., P.F., T.M., M.S., A.J.R., S.M., R.R., A.M.R., J.M.L., J.E.S., I.G., and L.W.M. analyzed data; and T.Y.K. and L.W.M. wrote the paper.

1. R. Ramesh, N. A. Spaldin, Multiferroics: Progress and prospects in thin films. *Nat. Mater.* **6**, 21–29 (2007).
2. N. A. Spaldin, R. Ramesh, Advances in magnetoelectric multiferroics. *Nat. Mater.* **18**, 203–212 (2019).
3. Y. H. Chu *et al.*, Electric-field control of local ferromagnetism using a magnetoelectric multiferroic. *Nat. Mater.* **7**, 478–482 (2008).
4. H. Béa *et al.*, Influence of parasitic phases on the properties of $BiFeO_3$ epitaxial thin films. *Appl. Phys. Lett.* **87**, 072508 (2005).
5. S. Dong *et al.*, Exchange bias driven by the Dzyaloshinskii-Moriya interaction and ferroelectric polarization at G-type antiferromagnetic perovskite interfaces. *Phys. Rev. Lett.* **103**, 127201 (2009).
6. Nature Nanotechnology, Memory with a spin. *Nat. Nanotechnol.* 10, 185 (2015), 10.1038/nnano.2015.50.
7. D. Lebeugle, A. Mougin, M. Viret, D. Colson, L. Ranno, Electric field switching of the magnetic anisotropy of a ferromagnetic layer exchange coupled to the multiferroic compound $BiFeO_3$. *Phys. Rev. Lett.* **103**, 257601 (2009).
8. S. M. Wu *et al.*, Reversible electric control of exchange bias in a multiferroic field-effect device. *Nat. Mater.* **9**, 756–761 (2010).
9. Y. H. Chu *et al.*, Electric-field control of local ferromagnetism using a magnetoelectric multiferroic. *Nat. Mater.* **7**, 478–482 (2008).
10. J. Allibe *et al.*, Room temperature electrical manipulation of giant magnetoresistance in spin valves exchange-biased with $BiFeO_3$. *Nano Lett.* **12**, 1141–1145 (2012).
11. R. Mahesh, P. V. Reddy, A study of ferroelectric and magnetic properties of rare earth (RE= La, Nd, Sm, Gd) doped $BiFeO_3$ using modified Becke Johnson potential with SOC techniques. *Mater. Chem. Phys.* **232**, 460–470 (2019).
12. D. Sando, A. Barthélémy, M. Bibes, $BiFeO_3$ epitaxial thin films and devices: past, present and future. *J. Phys.: Condens. Matter.* **26**, 473201 (2014).
13. J. C. Yang *et al.*, Orthorhombic $BiFeO_3$. *Phys. Rev. Lett.* **109**, 247606 (2012).
14. R. J. Zeches *et al.*, A Strain-driven morphotropic phase boundary in $BiFeO_3$. *Science* **326**, 977–980 (2009).

15. A. R. Damodaran *et al.*, Nanoscale structure and mechanism for enhanced electromechanical response of highly strained $BiFeO_3$ thin films. *Advanced Materials* **23**, 3170–3175 (2011).
16. Z. Chen *et al.*, Coexistence of ferroelectric triclinic phases in highly strained $BiFeO_3$ films. *Physical Review B*. **84**, 094116 (2011).
17. C. Ederer, N. A. Spaldin, Effect of epitaxial strain on the spontaneous polarization of thin film ferroelectrics. *Phys. Rev. Lett.* **95**, 257601 (2005).
18. A. R. Damodaran *et al.*, Temperature and thickness evolution and epitaxial breakdown in highly strained $BiFeO_3$ thin films. *Phys. Rev. B* **85**, 024113 (2012).
19. D. Sando *et al.*, Designer defect stabilization of the super tetragonal phase in >70-nm-thick $BiFeO_3$ films on $LaAlO_3$ substrates. *Jpn. J. Appl. Phys.* **57**, 0902B2 (2018).
20. D. Kan *et al.*, Universal behavior and electric-field-induced structural transition in rare-earth-substituted $BiFeO_3$. *Adv. Funct. Mater.* **20**, 1108–1115 (2010).
21. J. Z. Huang, Y. Shen, M. Li, C. W. Nan, Structural transitions and enhanced ferroelectricity in Ca and Mn co-doped $BiFeO_3$ thin films. *J. Appl. Phys.* **110**, 094106 (2011).
22. D. Kan, C.-J. Cheng, V. Nagarajan, I. Takeuchi, Composition and temperature-induced structural evolution in La, Sm, and Dy substituted $BiFeO_3$ epitaxial thin films at morphotropic phase boundaries. *J. Appl. Phys*. **110**, 014106 (2011).
23. D. Wang *et al.*, $BiFeO_3$-$BaTiO_3$: A new generation of lead-free electroceramics. *J. Adv. Dielectr.* **8**, 1830004 (2018).
24. T. Wang *et al.*, Large enhancement of properties in strained lead-free multiferroic solid solutions with strong deviation from Vegard's law. *Matter* **8**, 101874 (2024).
25. H. Zhao *et al.*, Ferroelectric, ferromagnetic and magneto-capacitance properties of Sm-doped $BiFeO_3$-$BaTiO_3$ solid solution. *Appl. Phys. A Mater. Sci. Process.* **129**, 77 (2023).
26. T. J. Park *et al.*, Composition-dependent magnetic properties of $BiFeO_3$-$BaTiO_3$ solid solution nanostructures. *Phys. Rev. B* **82**, 024431 (2010).
27. A. J. Preethi, M. Ragam, Effect of doping in multiferroic BFO: A review. *J. Adv. Dielectr.* **11**, 2130001 (2021).
28. R. Das, S. Sharma, K. Mandal, Aliovalent Ba^{2+} doping: A way to reduce oxygen vacancy in multiferroic $BiFeO_3$. *J. Magn. Magn. Mater.* **401**, 129–137 (2016).
29. J. Wang *et al.*, Epitaxial $BiFeO_3$ multiferroic thin film heterostructures. *Science* **299**, 1719–1722 (2003).
30. L. Chen *et al.*, Electrical and mechanical switching of ferroelectric polarization in the 70 nm $BiFeO_3$ film. *Sci. Rep.* **6**, 19092 (2016).
31. Q. Shi *et al.*, The role of lattice dynamics in ferroelectric switching. *Nat. Commun.* **13**, 1110 (2022).
32. R. Xu *et al.*, Kinetic control of tunable multi-state switching in ferroelectric thin films. *Nat. Commun.* **10**, 1282 (2019).
33. R. Xu *et al.*, Ferroelectric polarization reversal via successive ferroelastic transitions. *Nat. Mater.* **14**, 79–86 (2015).
34. Q. M. Zhang, H. Wang, N. Kim, L. E. Cross, Direct evaluation of domain-wall and intrinsic contributions to the dielectric and piezoelectric response and their temperature dependence on lead zirconate-titanate ceramics. *J. Appl. Phys.* **75**, 454–459 (1994).
35. D. Pantel *et al.*, Switching kinetics in epitaxial $BiFeO_3$ thin films. *J. Appl. Phys.* **107**, 084111 (2010).
36. Z. Chen *et al.*, Complex strain evolution of polar and magnetic order in multiferroic $BiFeO_3$ thin films. *Nat. Commun.* **9**, 3764 (2018).
37. J. J. Wang *et al.*, Magnetization reversal by out-of-plane voltage in $BiFeO_3$-based multiferroic heterostructures. *Sci. Rep.* **5**, 10459 (2015).
38. D. Chen *et al.*, A strain-driven antiferroelectric-to-ferroelectric phase transition in La-doped $BiFeO_3$ thin films on Si. *Nano Lett.* **17**, 5823–5829 (2017).
39. Z. Chen *et al.*, Complex strain evolution of polar and magnetic order in multiferroic $BiFeO_3$ thin films. *Nat. Commun.* **9**, 3764 (2018).
40. D. Alders *et al.*, Temperature and thickness dependence of magnetic moments in NiO epitaxial films. *Phys. Rev. B* **57**, 11623 (1998).
41. H. Zhong *et al.*, Quantitative imaging of exotic antiferromagnetic spin cycloids in $BiFeO_3$ thin films. *Phys. Rev. Appl.* **17**, 044051 (2022).
42. A. Haykal *et al.*, Antiferromagnetic textures in $BiFeO_3$ controlled by strain and electric field. *Nat. Commun.* **11**, 1704 (2020).
43. I. Gross *et al.*, Real-space imaging of non-collinear antiferromagnetic order with a single-spin magnetometer. *Nature* **549**, 252–256 (2017).
44. R. Witte *et al.*, High-entropy oxides: An emerging prospect for magnetic rare-earth transition metal perovskites. *Phys. Rev. Mater.* **3**, 034406 (2019).
45. R. Gupta, R. K. Kotnala, A review on current status and mechanisms of room-temperature magnetoelectric coupling in multiferroics for device applications. *J. Mater. Sci.* **57**, 12710–12737 (2022).
46. C. Zhang *et al.*, Optimizing nonrigid registration for scanning transmission electron microscopy image series. *Microsc. Microanal. Microstruct.* **27**, 90–98 (2021).
47. P. Appel *et al.*, Fabrication of all diamond scanning probes for nanoscale magnetometry. *Rev. Sci. Instrum.* **87**, 063703 (2016).
48. P. Maletinsky *et al.*, A robust scanning diamond sensor for nanoscale imaging with single nitrogen-vacancy centres. *Nat. Nanotechnol.* **7**, 320–324 (2012).
49. G. Srinivasan *et al.*, Magnetoelectric bilayer and multilayer structures of magnetostrictive and piezoelectric oxides. *Phys. Rev. B* **64**, 214408 (2001).
50. G. Srinivasan, E. T. Rasmussen, B. J. Levin, R. Hayes, Magnetoelectric effects in bilayers and multilayers of magnetostrictive and piezoelectric perovskite oxides. *Phys. Rev. B* **65**, 134402 (2002).
51. G. V. Duong, R. Groessinger, M. Schoenhart, D. Bueno-Basques, The lock-in technique for studying magnetoelectric effect. *J. Magn. Magn. Mater.* **316**, 390–393 (2007).
52. M. Hassanpour Amiri, H. Sharifi Dehsari, K. Asadi, Magnetoelectric coupling coefficient in multiferroic capacitors: Fact vs Artifacts. *J. Appl. Phys.* **132**, 164102 (2022).
53. K. F. Garrity *et al.*, Pseudopotentials for high-throughput DFT calculations. *Comput. Mater. Sci.* **81**, 446–452 (2014).
54. J. B. Neaton *et al.*, First-principles study of spontaneous polarization in multiferroic $BiFeO_3$. *Phys. Rev. B* **71**, 014113 (2005).
55. S. L. Dudarev *et al.*, Electron-energy-loss spectra and the structural stability of nickel oxide: An LSDA+U study. *Phys. Rev. B* **57**, 1505 (1998).
56. A. Singh, A. Senyshyn, H. Fuess, S. J. Kennedy, D. Pandey, Magnetic transitions and site-disordered induced weak ferromagnetism in (1–x)$BiFeO_3$-x$BaTiO_3$. *Phys. Rev. B* **89**, 024108 (2014).